

Influence of water saturation and water memory on CO₂ hydrate formation/dissociation in porous media under flowing condition

Aghajanloo, Mahnaz; Taghinejad, Sadegh M.; Voskov, Denis; Farajzadeh, Rouhi

DOI

[10.1016/j.cej.2024.152455](https://doi.org/10.1016/j.cej.2024.152455)

Publication date

2024

Document Version

Final published version

Published in

Chemical Engineering Journal

Citation (APA)

Aghajanloo, M., Taghinejad, S. M., Voskov, D., & Farajzadeh, R. (2024). Influence of water saturation and water memory on CO₂ hydrate formation/dissociation in porous media under flowing condition. *Chemical Engineering Journal*, 492, Article 152455. <https://doi.org/10.1016/j.cej.2024.152455>

Important note

To cite this publication, please use the final published version (if applicable). Please check the document version above.

Copyright

Other than for strictly personal use, it is not permitted to download, forward or distribute the text or part of it, without the consent of the author(s) and/or copyright holder(s), unless the work is under an open content license such as Creative Commons.

Takedown policy

Please contact us and provide details if you believe this document breaches copyrights. We will remove access to the work immediately and investigate your claim.



Influence of water saturation and water memory on CO₂ hydrate formation/dissociation in porous media under flowing condition

Mahnaz Aghajanloo^{a,*}, Sadegh M. Taghinejad^a, Denis Voskov^{a,b}, Rouhi Farajzadeh^{a,c}

^a Delft University of Technology, Department of Geoscience and Engineering, Stevinweg 1 2628 CN, Delft, the Netherlands

^b Department of Energy Science and Engineering, Stanford University, 367 Panama street, CA 94305, United States

^c Shell Global Solutions International B.V., Grasweg 31 1031 HW Amsterdam, the Netherlands

ARTICLE INFO

Keywords:

Water Saturation
Porous Media
Hydrate Formation/Dissociation Cycle
Water Memory Effect
CO₂ Hydrate Kinetic
Permeability
X-ray CT scan

ABSTRACT

Injection of high-pressure CO₂ into depleted gas reservoirs can lead to low temperatures promoting formation of hydrate in the near wellbore area resulting in reduced injection rates. The design of effective mitigation methods requires an understanding of the impact of crucial parameters on the formation and dissociation of CO₂ hydrate within the porous medium under flowing conditions. This study investigates the influence of water saturation (ranging from 20 % to 40 %) on the saturation and kinetics of CO₂ hydrate during continuous CO₂ injection. The experiments were conducted under a medical X-ray computed tomography (CT) to monitor the dynamics of hydrate growth inside the core and to calculate the hydrate saturation profile. The experimental data reveal increase in CO₂ hydrate saturation with increasing water saturation levels. The extent of permeability reduction is strongly dependent on the initial water saturation: beyond a certain water saturation the core is fully blocked. For water saturations representative of the depleted gas fields, although the amount of generated hydrate is not sufficient to fully block the CO₂ flow path, a significant reduction in permeability (approximately 80 %) is measured. It is also observed that the volume of water + hydrate phases increases during hydrate formation, indicating a lower-than-water density for CO₂ hydrate. Having a history of hydrate at the same water saturation leads to an increase in CO₂ consumption compared to the primary formation of hydrate, confirming the existence of the water memory effect in porous media.

1. Introduction

Carbon dioxide (CO₂) emissions from anthropogenic sources are a major contributor to the rapid rise in global temperature and the subsequent effects of climate change, which will indeed have substantial implications for future life on Earth [1–3]. Considering the ongoing reliance on fossil fuels for energy generation, the adoption of carbon capture and storage (CCS) is increasingly acknowledged as a highly promising technology to mitigate the environmental impacts of CO₂ emissions [4,5].

Among the diverse geological formations applicable for CO₂ storage, gas-depleted fields hold distinct advantages and offer substantial secure and long-term storage capacity [6–10]. Nevertheless, in depleted low-pressure reservoirs, the introduction of high pressure condensed CO₂ during injection can lead to substantial adiabatic expansion, a phenomenon known as Joule-Thomson cooling (JTC), particularly within the well-tubing or the near wellbore region. This is mainly attributed to

the establishment of significant pressure gradients [11]. A notable concern associated with this phenomenon is the potential for CO₂ hydrate generation when CO₂ interacts with the residual water during the injection phase [12,13]. This CO₂ hydrate formation pose flow assurance challenges and potentially compromise the functionality of the injection well Aghajanloo et al. [14], Chesnokov and a. F., Rouhi and Kahrobaei, Siavash and Snippe, Jeroen and Bedrikovetski, Pavel, [15].

Many publications on CO₂ injection in depleted gas reservoirs have addressed different aspects on the CO₂ phase transition (CO₂ hydrate formation) within the wellbore such as impact of CO₂ flow characteristic [12], CO₂ pretreatment [16], salinity of formation water [17,18], salt precipitation [19,20], and rock mineralogy and permeability [21], aiming to assess and mitigate this operational risk. Nevertheless, there has been no exploration into how reservoir water content (water saturation), and the water memory (refers to the phenomenon where previous hydrate formation experiences an impact on subsequent nucleation) impact the CO₂ hydrate formation and saturation under flowing conditions [22]. Research demonstrate that at high water

* Corresponding author.

E-mail address: m.aghajanloo@tudelft.nl (M. Aghajanloo).

<https://doi.org/10.1016/j.cej.2024.152455>

Received 17 February 2024; Received in revised form 18 May 2024; Accepted 20 May 2024

Available online 21 May 2024

1385-8947/© 2024 The Author(s). Published by Elsevier B.V. This is an open access article under the CC BY license (<http://creativecommons.org/licenses/by/4.0/>).

Nomenclature			
BP	Back Pressure	PT	Pressure Transducer
c	Chen model constant	R	universal gas constant
CCS	Carbon Capture and Storage	r_{CO_2}	CO ₂ consumption rate [mole/min]
CH	Core Holder	S_H	hydrate saturation [%]
CP	Confining Pressure	S_w	water saturation [%]
CPA	Cubic-Plus-Association	t	time [s]
CT	Computed Tomography	T	Temperature
CT _{dry}	CT number of dry core [HU]	TC	Thermocouple
CT _{exp}	CT number during experiment [HU]	TJ	Thermal Jacket
CT _{wet}	CT number of fully wet core [HU]	V	Volume, [ml]
DP	Differential Pressure	V _H	volume of hydrate [ml]
E	Experiment	V _φ	volume of core porosity [ml]
EoS	Equation of State	z	compressibility factor
f _{conv}	water conversion [%]	<i>Greek Character</i>	
JTC	Joule-Thomson Cooling	β	Pang-Sharma model constant
k	permeability [D]	φ	porosity
MeOH	Methanol	ρ	density of hydrate [g/ml]
MFC	Mass Flow Controller	Δ	difference
m _H	mass of hydrate [g]	<i>Subscript & Superscript</i>	
Mw	molecular weight [g/mol]	H	hydrate
NH	hydration number	inj	injection
n	number of moles [mol]	m	mole
n _t	moles of CO ₂ at time t [mol]	t	time
n _{H₂O}	total mole of water [mol]	w	water
P	pressure		

saturation region, where the porous medium is predominantly filled with water (>90 %), the formation of gas hydrates can be constrained due to the limited availability of a gas phase Wang et al. [23]. Conversely, low water saturations with substantial gas content are more favorable for gas hydrate formation [24]. Furthermore, gas hydrate dissociation is an endothermic process, that requires heat to dissociate the hydrate structure to release gas molecules. This energy can be supplied from the surrounding pore area. This cooling effect may promote the reformation of the new gas hydrates, especially in the presence of water memory effect and continuous supply of gas molecules Aghajanloo et al. [14]. To assess the feasibility of CO₂ storage in depleted reservoirs, quantifying the impact of different water saturations in the presence/absence of water memory on CO₂ hydrate volume/saturation is required to identify under which condition hydrate is more stable and the effect of hydrate on injectivity becomes detrimental for CCS projects [25].

Hence, this study aims to present insights into the influence of water saturation levels on the volume of CO₂ hydrate and the resulting permeability changes in a Bentheimer core. The Bentheimer sandstone core is selected for the experimental investigations due to its homogeneity, consistent mineralogy, low clay content, and high permeability. The core flood experiments were conducted under isothermal condition of 273.65 K, with the initial pressure set at 3 MPa. This pressure is chosen as a representative value for the candidate depleted gas field in the North sea [26] while the temperature is assumed to be reached by the Joule-Thompson cooling happening due to the expansion of the cold liquid CO₂ injected into the reservoir. The study also provided an opportunity to assess whether the water memory can influence the kinetics of CO₂ hydrate such as CO₂ consumption rate and induction time within porous media. Furthermore, the study applied X-ray CT scanning to characterize and quantify water/hydrate saturation and distribution along the core during dynamic CO₂ injection, particularly at three initial water saturation levels.

2. Experimental section

2.1. Material

The CO₂ as hydrate former and N₂ had a certified purity respectively 99.7 % and 99.999 %, were sourced from Linde Co. gas supplier. The electrolyte (NaCl) was of certified 99.5-grade provided by Fisher Scientific. Deionized distilled water was used to prepare the brine solutions. Cylindrical outcrop Bentheimer core plugs were used as porous media in all the experiments. These core had dimensions of 3.8 cm in diameter, 17 cm in length, a porosity (φ) of 0.23, and permeability (K) ranging from 2.2 to 2.5 D.

2.2. Experimental setup

The schematic of the experimental setup applied for core-flood experiments is depicted in Fig. 1. This includes a Bentheimer sand rock coated with a 5 mm thick layer of epoxy resin to provide a protective barrier for the fluids. The sand core is located inside a polyetheretherketone (PEEK) core holder, which is designed to maintain containment at high pressure and low temperature. Four pressure transducers are employed to measure pressure changes at the: inlet, 2.25 cm from the inlet, 6.5 cm from the outlet, and outlet (GE UNIK 5000— Accuracy to ± 0.04 % Full Scale, ranges from 0.007 to 8 MPa). Two differential pressure devices (Endress and Hauser, Deltabar S, ranges: −0.03 to + 0.03 MPa) are utilized to acquire the pressure difference at the other two locations. Two thermocouples are placed inside the core and at the core outlet to measure local temperatures. A high-pressure control system, typically referred to as the back pressure system, is linked to the outlet of the core holder. The back pressure is adjusted with a large N₂ cylinder to sustain the specific pressure of the experiments (3 MPa). The effluent solution is accumulated in an adsorbent-equipped vessel. A data acquisition system is responsible for collecting and adjusting various parameters such as temperature and pressure within the system. This includes a pulse-free high-precision

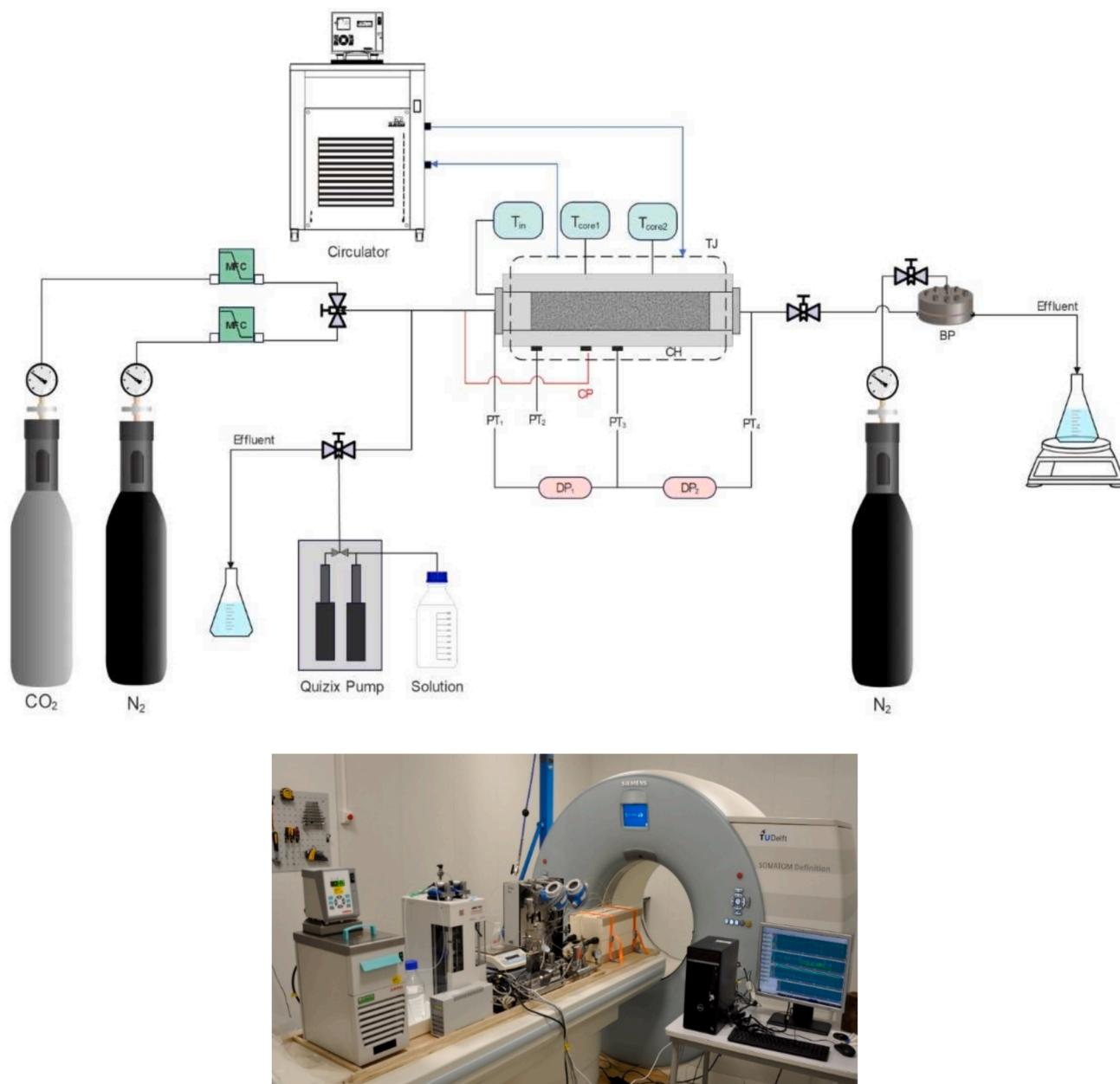


Fig. 1. Schematic diagram and photo of the laboratory apparatus. (BP) Back Pressure; (CH) Core Holder; (CP) Confining Pressure; (DP) Differential Pressure; (MFC) Mass Flow Controller; (PT) Pressure Transducer; (TC) Thermocouple; Thermal Jacket.

piston pump (Quizix QX-6000HC) for driving solutions from the vessel into the core holder and a high-pressure gas mass flow controller (Bronkhorst F-230 M) to manage the injection rate of gas flowrate. The inlet line between the pumps and the inlet end-cap is kept long to equilibrate the water and gas before entering the core. The effluent is collected in a 500 ml collection vessel. The core holder is enveloped by a cooling jacket where the cooling medium is continuously circulated through the jacket using a circulator (LAUDA Proline RP845). The precision of the circulator is within ± 0.1 K. A medical X-ray CT-scan instrument (Siemens Somatom Volume) is used to compute fluid saturation levels and hydrate volume during the formation/dissociation process. The slice thickness for each scan is 0.6 mm, while a resolution of 0.2 mm in the other two dimensions, leads to a voxel size of $0.2 \times 0.2 \times 0.6 \text{ mm}^3$. A voltage of 140 kV and a current of 250 mA is employed.

2.3. Experimental procedure

2.3.1. Water saturation

The experiments involved the measurement of water saturation, hydrate nucleation time and hydrate saturation by conducting core-flood tests on a homogenous Bentheim sandstone. To quantify the water/hydrate distribution within the rock core, a medical X-ray CT scanner was employed. To achieve a uniform water saturation below 40 % in the core, a modified gas/water co-injection technique was utilized [27]. In brief, the process began with the injection of N_2 into the system, gradually rising the pressure by 0.5 MPa increments up to a target pressure of 3 MPa. Confining pressure was set equal to the injection pressure. Subsequently, a degassed solution consisting of 1 wt% NaCl and deionized water with N_2 was simultaneously introduced into the vertical core using a specific fractional flow under constant temperature of 273.65 K. The total flow rate, which included both gas and liquid flow, was maintained at 6 ml/min. The ratio of brine to N_2 was

regulated using a Quizix pump and a mass flow controller.

2.3.2. Hydrate formation/dissociation cycle

Following the establishment of the desired water saturation, CO₂ injection into the core commenced at a constant velocity of 1 ml/min. The initial pressures selected for hydrate formation in all experimental runs were set at 3 MPa, while the temperature was maintained at 273.65 ± 0.5 K (~6 degree of subcooling based on CO₂/water P-T phase diagram shown in Fig. 2). This consistent temperature and pressure were chosen to create a controlled environment closely resembling real-reservoir conditions where CO₂ hydrates can potentially form. This allowed for precise observations and measurements of CO₂ hydrate behavior under specific operating conditions. Cyclic tests were conducted to investigate whether the presence of water memory influences subsequent hydrate nucleation.

The experimental procedure encompassed CO₂ hydrate formation until a steady state was achieved, after which dissociation was initiated. The first three cycles involved thermal stimulation as a method for hydrate decomposition. This approach ensured the retention of the same solution for subsequent cycles. However, for some experiments, a solution containing methanol (MeOH) was introduced to assess the effectiveness of MeOH as a hydrate remediator to decompose the hydrate structure. Chemical solutions were prepared at loadings of 15 wt% MeOH with degassed deionized water containing 1 wt% NaCl. Considering that both temperature and duration of heating impact the water memory effect, surpassing a particular temperature threshold or exceeding a specific duration of heating can lead to a rapid decrease or complete disappearance of water memory [28]. In this study, during the hydrate dissociation process induced by thermal stimulation, the temperature remained below 293.15 K, and the dissociation process was limited to within a day to prevent the elimination of the water memory associated with hydrates.

• CO₂ Consumption and Hydrate Formation Rate

The data acquisition system recorded the pressures and temperatures inside the core sample every 10 s. The calculated CO₂ consumption

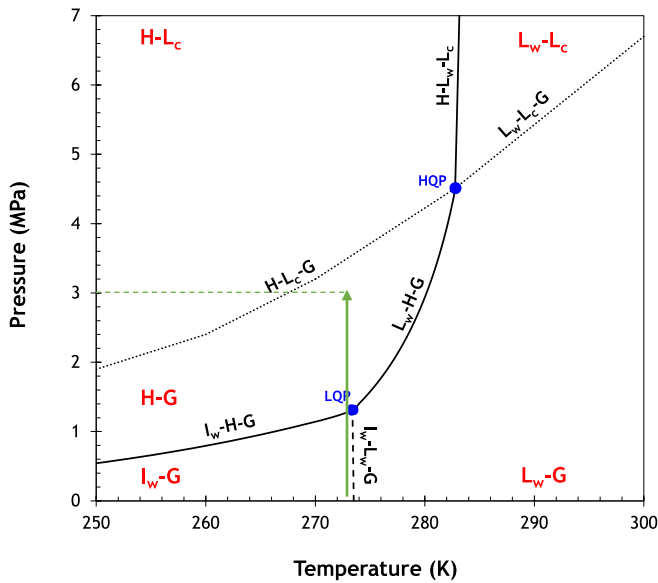


Fig. 2. Three-phase diagram of the CO₂-water mixture. The symbols I_w, L_c, L_w, H, and G represent ice water, liquid CO₂, liquid water, hydrate, and gas, respectively. HQP and LQP refer to high (L_wHL_cG) and low (I_wHL_wG) quadruple points. The smooth line represent the three-phase equilibrium line, the dotted line indicate the CO₂ condensed line, and the dashed line is ice line. (HydraFLASH version 3.8, CPA EoS).

(total moles of CO₂ consumed from the gas phase) at any given time (t) was determined as a function of the compressibility factor. The calculations were made based on an assumption regarding gas consumption (Δn), which was defined as the difference in the amount of CO₂ introduced into the core at time t (n_t) and the amount of CO₂ that exited the core at next time step ($n_t + \Delta t$). This estimation can be expressed as follows:

$$n_t = \left(\frac{PV}{ZRT} \right)_t \quad (1)$$

$$\Delta n = \sum_0^t (n_t - n_{t-\Delta t}) \quad (2)$$

where P represents the pressure inside the core, V stands for gas volume, T is the temperature, and the universal gas constant is expressed as R . The compressibility factor (z) was calculated iteratively through the Cubic-Plus-Association (CPA) equation of state (EoS) using HydraFLASH software version 3.8. In equation (2), $t = 0$ denotes the initial condition (just before the CO₂ injection), and $t > 0$ represents time during CO₂ injection.

From kinetic perspective, the CO₂ hydrate formation process encompasses the diffusion of dissolved gas from the aqueous phase to the interface of the hydrate crystal and brine, where the CO₂ molecules are integrated into the clathrate structure. To quantify the rate of CO₂ hydrate formation in dynamic conditions, the moles of CO₂ consumed were utilized. The rate of change in CO₂ gas moles at each time yields the formation rate. This was computed using the following equation:

$$r_{CO_2} = \left(\frac{dn_t}{dt} \right)_{t-\Delta t, t} \quad (3)$$

Where r is the CO₂ hydrate formation rate. Δn is the difference in the number of moles of CO₂ gas. Δt is the time interval.

• CO₂ Hydrate Saturation

The total mass of hydrate formation [29] was obtained applying following equation:

$$m_H = f_{conv} \times n_{H_2O} \left[Mw^{H_2O} + \frac{Mw^{CO_2}}{NH} \right] \quad (4)$$

where f_{conv} denotes the fraction of water converted to hydrate, estimated from HydraFLASH software, considering water content (water saturation) and thermodynamic conditions specific to each experiment. The term n_{H_2O} is the total moles of water inside the core, and Mw^{H_2O} and Mw^{CO_2} are water and CO₂ molecular weight, respectively. Hydration number (NH) is the average number of water per gas molecule in a unit structure sl.

Hydrate saturation (S_H), was determined by calculating the volume of hydrate normalized to the pore volume of the core (V_ϕ). This calculation was carried out using the following equation:

$$S_H (\%) = \frac{V_H}{V_\phi} = \frac{m_H}{V_\phi \times \rho_H} \quad (5)$$

where V_H and ρ_H is the volume and density of hydrate defined by the following relationship:

$$\rho_H = \frac{m_H}{V_H} \quad (6)$$

To calculate water and hydrate saturations [30], CT images of the core were obtained under both fully brine-saturated (CT_{wet}) and dry (CT_{dry}) conditions. The saturation was calculated using the following equation [31]:

$$S_{w/H} = \frac{CT_{exp} - CT_{dry}}{CT_{wet} - CT_{dry}} \quad (7)$$

where, CT_{exp} represents the voxel level CT number for the core at various steps throughout the experiment, encompassing water saturation, CO_2 injection, CO_2 hydrate formation, and dissociation.

3. Results and discussion

3.1. Impact of water saturation and water memory on CO_2 hydrate saturation

A significant risk to injectivity during CO_2 storage is the potential for hydrate formation near wellbore area [16,21]. Consequently, when investigating the impact of hydrate, multiple factors need to be considered, including thermodynamic condition (T and P), salinity, and water saturation Wang et al. [32]. Depleted gas reservoir typically exhibit low water saturations; however, aquifer influx and water mobilized by capillary pressure can pull back water near wellbore area. Moreover, in a heterogeneous reservoir different layer may contain different levels of water saturation. Hence, it is essential to quantify impact of water saturation on extent of injectivity decline and dynamics of hydrate formation/dissociation.

To gain insight into the experimental findings, the initial step involved prediction of hydrate saturation (referring to the maximum water-to-hydrate conversion under given thermodynamic conditions) corresponding to water saturations ranging from 20 % to 60 % at 3 MPa using HydraFLASH software, applying the CPA EoS. Fig. 3 presents the linear correlation between hydrate volume/hydrate saturation and water saturation. The slope of the line in this figure is calculated to be 1.21, with > 0.97 % water-to-hydrate conversion efficiency, indicating that CO_2 hydrate structure sl occupies 21 % more pore volume compared to water under assumed conditions. With hydration number of ~ 5.9 to 6.1, the estimated hydrate density is ~ 0.804 g/ml. This estimation assumes a uniform distribution of water and CO_2 and ignores the potential coexistence of ice due to nonuniformity, which may exist in a real system. Accordingly, in the studied range of water saturations (20 % – 60 %), when excess CO_2 is present, the efficiency of water-to-hydrate conversion remains constant across the specified water saturation levels. However, as depicted in Fig. 4, under a constant pressure of 3 MPa, the latent heat (enthalpy) of CO_2 hydrate formation decreasing from 396.7 kJ/kg with water saturation above 20 %. Additionally, the

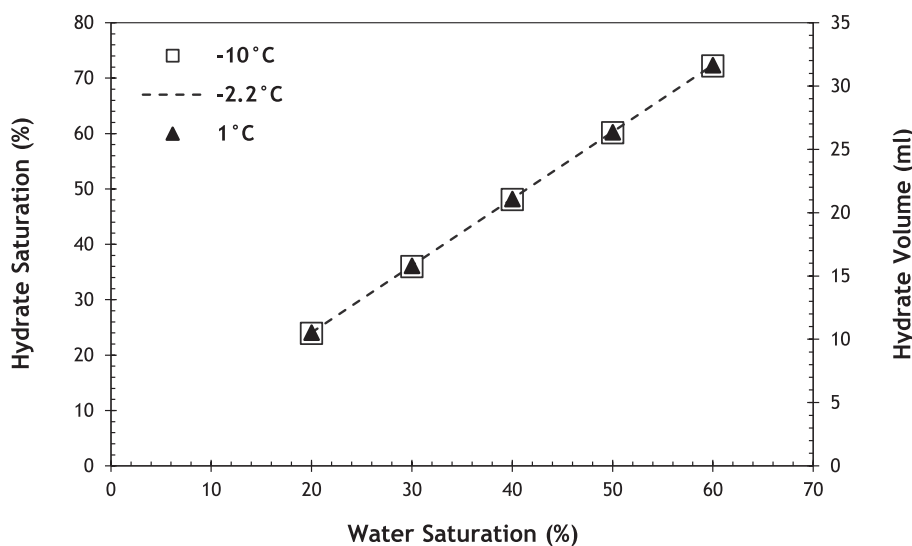


Fig. 3. Relation between water saturation, hydrate saturation and hydrate volume at $P = 3$ MPa for different temperatures. At $T = 263.15$ K, no ice formation was assumed. The density of the hydrate was calculated as 0.803 ± 0.0001 g/ml. (HydraFLASH version 3.8, CPA EoS).

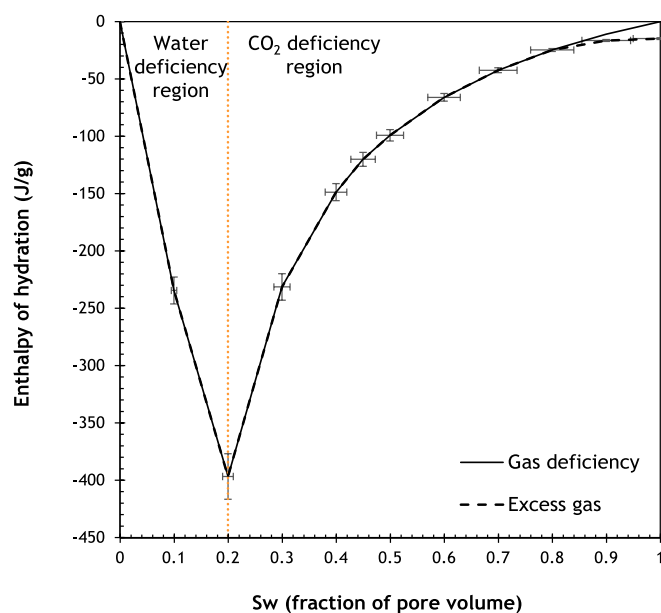


Fig. 4. Latent heat of hydrate formation in different water saturation at $P = 3$ MPa in presence/absence of excess CO_2 . (HydraFLASH version 3.8, CPA EoS).

influence of water saturation on hydrate saturation is different when hydrate coexists with ice at lower temperatures. The simulation results also indicate that when the reservoir conditions are situated within the hydrate stability region, at a constant pressure the temperature has a relatively low impact on hydrate saturation during CO_2 injection. This limited influence of temperature can be attributed to the constant density of CO_2 in the gas phase (due to continuous CO_2 injection), leading to the saturation of water with CO_2 . Consequently, the hydrate lattice stabilizes upon achieving maximum CO_2 filling. Consequently, additional temperature change does not significantly alter the encapsulation of CO_2 , a crucial factor for hydrate stabilization. For these calculations, at $S_w = 0.81$, hydrate will fully occupy the porous medium. However, flow of CO_2 will be hindered if hydrate saturation reaches a specific value and therefore formation of hydrate will be limited due to inaccessibility of CO_2 .

Fig. 5 (a) depicts the pressure and temperature data throughout four cycles of CO_2 hydrate formation and dissociation from a sample

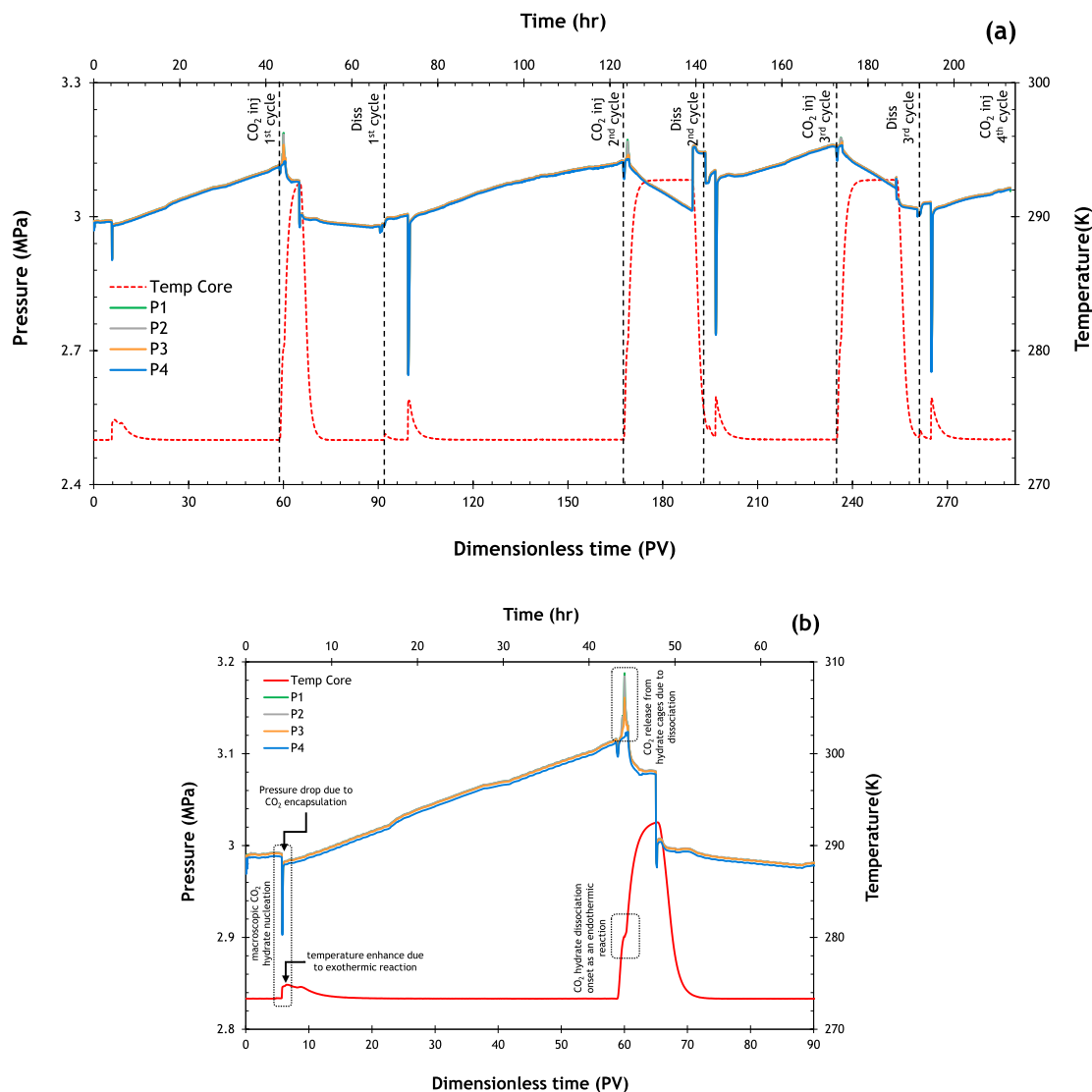


Fig. 5. Pressure and temperature profile during CO₂ hydrate formation and dissociation cycles (a), focused on the first cycle (b), for $S_w = 42.1\%$ containing 1 wt% NaCl. Initial condition: 3 MPa; and 273.65 K. Pressure changes were monitored at the inlet (P₁), 2.25 cm from the inlet (P₂), 6.5 cm from the outlet (P₃), and the outlet (P₄).

experiment of 41.2 % water saturation (E8). CO₂ injection commenced in the first cycle following the saturation of the sand core with 1 wt% NaCl brine. The primary sign of hydrate formation was macroscopically detected at induction time, characterized by a simultaneous pressure drop due to CO₂ encapsulation within the hydrate cavities and a temperature increase resulting from the exothermic hydrate formation reaction (see Fig. 5 (b)). Following the induction period, pressures gradually increased, corresponding to the progress in hydrate growth during CO₂ injection. Despite this volume increase causing a reduction in porosity and permeability, leading to increased pressure, no blockage was recorded under these conditions. Moreover, this pressure increase also be attributed to the ongoing CO₂ injection, which resulted in hydrate cages trapping more CO₂ and thereby enhancing the stability of the hydrate structure. CO₂ injection persisted throughout each cycle until the thermodynamic conditions (P and T) reached a steady state. Thermal stimulation at 293.15 K was employed to dissociate the hydrate. Following the hydrate dissociation of the first cycle, water saturation decreased to 39.6 %, due to the production of 0.71 ml of water from the core (see Table 2). Subsequently, the system was cooled during N₂ injection, and the N₂ stream was replaced by the CO₂ upon reaching the desired subcooling (~6 degree of subcooling) to induce hydrate

formation of the next cycle.

Analysis of data from the four cycles (details reported in Table 2) indicated that the first cycle exhibited a significantly lower pressure drop at induction time (0.09 MPa) compared to subsequent cycles (approximately 0.36 MPa). This difference was attributed to the water memory effect, arising from the extensive release of CO₂ encapsulated within hydrate cages during the first hydrate dissociation, leading to the generation of gas bubbles. These CO₂ bubbles contributed to the sharpest pressure drop during subsequent hydrate pore filling. However, despite these pressure variations, final hydrate volume calculations based on water saturation levels did not indicate substantial differences across cycles.

Table 1 provides relevant data from four cycles of hydrate formation for five different distinct water saturations. The most significant pressure drop arising from the onset of hydrate formation (macroscopic induction time) was observed in the fourth cycle of E1, characterized by the lowest water saturation. The result implies that within the studied range of water saturation, the water saturation level of 22 % forms a more stable structure of CO₂ hydrate. This criticality might be attributed to a more uniform water distribution at this specific water saturation level, resulting in an improved water-gas interface and an increased

Table 1

Summary of phase saturations and hydrate formation results from five distinct water saturation at 273.65 K and initial pressure of 3 MPa.

Water saturation (%)	Water conversion ^a (%)	Induction Time (hr)	Temp change with hydrate formation	CO ₂ hydrate saturation ^b (%)	Blockage due to hydrate formation	CO ₂ hydrate volume (ml)
E1,1 (22.1)	74.4	0.8	1.97	19.8	–	8.80
E1,2 (19.9)	87.2	1.4	2.11	21.0	observed	9.25
E1,3 (19.9)	89.7	1.3	2.53	21.6	–	9.53
E1,4 (19.9)	95.5	3.1	3.06	23.0	–	10.12
E2,1 (25.9)	58.7	1.7	1.65	18.4	–	8.11
E2,2 (25.9)	76.9	1.3	1.38	24.1	–	10.64
E2,3 (25.9)	83.3	2.2	2.37	26.1	–	11.52
E2,4 (25.9)	77.9	1.1	2.01	24.4	–	10.74
E3,1 (30.1)	61.8	2.7	1.26	22.5	–	9.91
E3,2 (30.1)	90.6	5.9	3.07	33.0	–	14.56
E3,3 (30.1)	90.9	5.5	3.06	33.1	–	14.59
E3,4 (30.1)	91.4	11.2	2.27	33.3	–	14.70
E4,1 (32.2)	70.8	0.4	1.56	27.6	–	12.16
E4,2 (32.2)	87.5	1.3	2.45	34.1	–	15.04
E4,3 (32.2)	86.5	0.9	2.30	33.7	–	14.86
E4,4 (32.2)	92.7	6.8	3.08	36.1	–	15.9
E5,1 (35.1)	61.0	0.9	1.12	25.9	–	11.41
E5,2 (35.1)	85.9	0.5	3.11	36.5	observed	16.08
E5,3 (35.1)	63.3	0.3	2.78	26.9	observed	11.85
E5,4 (35.1)	89.9	1.7	3.32	38.2	–	16.83

^a hydration number = 6.2^b hydrate density ~ 0.803 g/ml

dissolution of CO₂. From another perspective, under the specified conditions (273.65 K and an initial pressure of 3 MPa, in the presence of water memory), the higher-pressure reduction observed in the fourth cycle contributes to the generation of a more stable hydrate, filled with the highest amount of CO₂. In this context, E3 with 30.1 % water

saturation, demonstrated the longest induction time across all cycles. This observation suggests that at this specific water saturation level, the hydrate nucleation process took the longest time compared to other saturation levels. Moreover, a positive correlation between the induction times (whether fresh or from memory) and the hydrate saturation

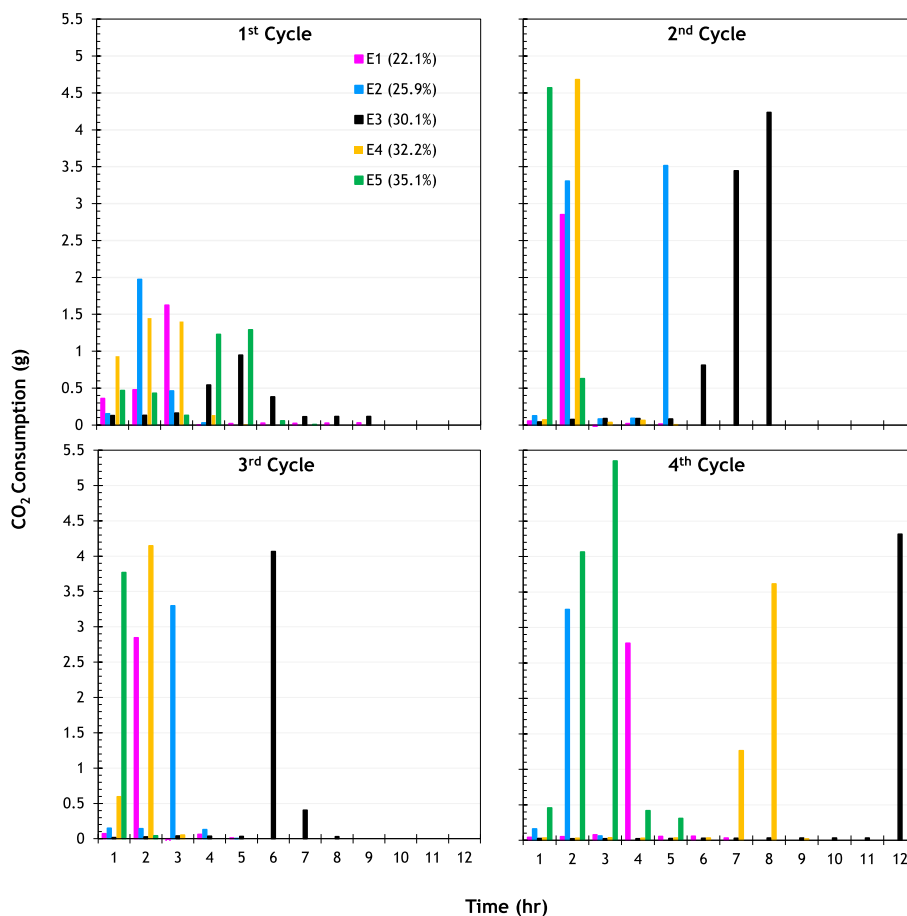


Fig. 6. Impact of water saturation and water memory on CO₂ consumption includes both CO₂ dissolution and hydrate formation during CO₂ injection. The data presented shows the CO₂ consumption rate per hour of CO₂ injection.

was evident in the obtained data. However, with an increase in water saturation, blockages in flow channels became apparent in certain secondary cycles, such as the second and third cycles in E5. This phenomenon led to a decline in permeability, confirming that the likelihood of blockage increases with hydrate re-formation. This could be attributed to the redistribution of water following hydrate dissociation. The pressure data recorded along the core length revealed that the blockage occurred in the end section of the core rock, which is likely associated with higher water saturation in that section due to displacement of water by CO₂. Based on the data provided in Table 1, slight variations in hydrate saturation (water-to-hydrate conversion) were observed among cases. However, across all water saturations, there was a consistent increase in conversion from the first cycle, which can be related to the memory effect. This implies that water memory not only accelerates hydrate nucleation but also influences hydrate density, possibly due to the residual structure hypothesis [33] and the guest supersaturation hypothesis [34]. Furthermore, findings show that during the primary hydrate formation, the synthesized CO₂ hydrate mainly occupies small pores, while in the secondary synthesis, it enters both small and large pores [35]. As a result, the CO₂ hydrate previously formed in the larger pores can impede the water in smaller pores from participating in the CO₂ hydrate formation process, creating a pore-blocking effect that was not observed in the second synthesis. Consequently, the calculated hydrate density was lower for the first cycle compared to the subsequent cycles.

As depicted in Fig. 6, it was observed that for cycles with identical initial water saturation, the average rate of secondary CO₂ consumption due to CO₂ dissolution and hydrate formation was 2.5 to 4 times greater than that observed in the primary formation. This trend was particularly pronounced at higher water saturations. To clarify, except for water saturations at 22 % and 25 %, in all cycles, the moles of CO₂ consumed were 1.5 times greater than in freshwater (the first cycle with no hydrate history). These findings suggest the presence of water memory during multicycle synthesis processes. Moreover, the findings reveal that during the primary synthesis, CO₂ predominantly occupies small pores, while in the secondary synthesis, it enters both small and large pores [35]. As a result, the CO₂ hydrate formed in the first cycle could exhibit a slightly lower density compared to the hydrate formed in the secondary synthesis. This difference in pore occupancy and distribution contributes to the observed density difference between the two synthesis cycles. The memory effect of hydrates has been elucidated through the proposal of various mechanistic hypotheses, including the residual structure hypothesis [36,37] and the guest supersaturation hypothesis [34]. Based on the residual structure hypothesis, it is assumed that after a cycle of formation and dissociation, the remaining structure retains the structural features of the hydrate phase. These residual cage structures serve as nucleation sites for the subsequent hydrate synthesis. However, the supersaturation hypothesis refers that by hydrate dissociation, dissolved gas molecules have a sufficiently small size, and the local pressure is sufficient to support gas bubble generation. The presence of these gas

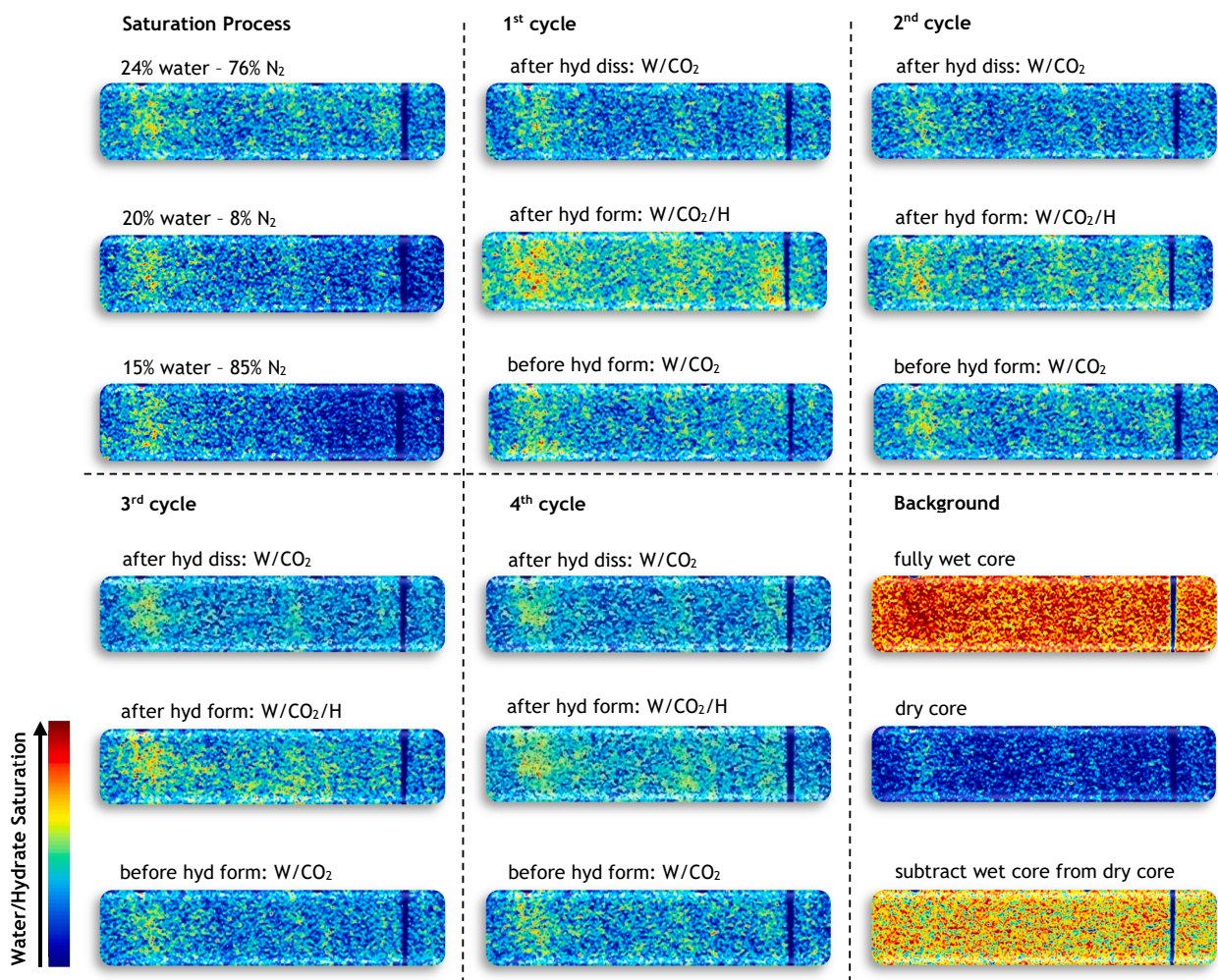


Fig. 7. Dynamic CT images of water/hydrate saturation maps during the water saturation process of a horizontal Bentheimer rock sample as well as during hydrate formation/dissociation cycles in E6. Flow direction is from left to right. (Colors qualitatively indicate water + hydrate saturation; red: high water/hydrate saturation; green/yellow: intermediate saturation; blue: low water/hydrate saturation).

bubbles facilitates the nucleation process for the subsequent hydrate formation [35].

Although the gas consumption rates increased with increasing water memory, E3 exhibited the highest CO₂ hydrate nucleation time among the studied cases.

3.2. Determination of Water/Hydrate saturations using CT-Scan

Medical X-ray CT scans were employed for three selected water saturation (24 %, 35 %, and 41 %) to evaluate water/hydrate distribution and quantify saturation throughout the core length during the hydrate formation/dissociation process. Given the resolution of medical CT images, and considering the similarity in density of water and CO₂ hydrate, it is very difficult to distinguish between these two phases through CT scanning.

Fig. 7 displays the CT scans from 24.3 % water saturation (E6), where the first section shows the fully saturated and dry core (background section). The three images located at the top left illustrate water saturation progress (water saturation change within the core sections during the water/N₂ co-injection). The remaining set of images in this figure depicts the pattern of water + hydrate saturation in three stages, including the conditions before and after hydrate formation, and after hydrate dissociation. In this figure, two high porosity zones are situated around 2.25 cm and 14.5 cm from the inlet, which are the locations of the pressure transducer (P₁) and the thermocouple (T_{core}), respectively. This increased porosity and permeability results in an accumulation of more water, leading to a higher saturation of hydrate within these core

sections.

Moreover, the CT images (Fig. 7) and the graph obtained from image analysis (Fig. 8) indicated a redistribution of water and hydrate along the core sections throughout hydrate growth, particularly in the third cycle. Furthermore, a comparison of water distribution across cycles confirmed that the hydrate dissociation process also altered the water distribution pattern. Based on Fig. 7, it is apparent that the hydrate saturation in the first cycle was slightly higher than the hydrate saturation observed in subsequent cycles. The observed slight decrease in hydrate saturation from the first cycle can be attributed to the influence of pore water redistribution on the rock surfaces [39] and the possible evaporation of water into the gas phase. This redistribution impacts the likelihood of hydrate nucleation, particularly in areas where the local water saturation on the rock surface is higher [40]. Another notable observation concluded from the cyclic tests on the Bentheimer core emphasizes the importance of the stochastic aspect of hydrate nucleation. Particularly under low subcooling conditions, serving as the hydrate driving force, hydrate nucleation is a stochastic process influenced by pore characteristics, salinity, and water history Lu et al. [33,41–43]. The experimental outcomes revealed that water level had the most significant impact on hydrate nucleation probability with 1 wt % salinity under consistent thermal history (water memory). However, in reservoir conditions where multiple conflicting aspects come into play, hydrate nucleation may be controlled by several factors [40].

To visualize the growth patterns of CO₂ hydrate in Bentheimer sandstone in the presence/absence of water memory, hydrate was repeatedly formed under a constant temperature of 273.65 K using

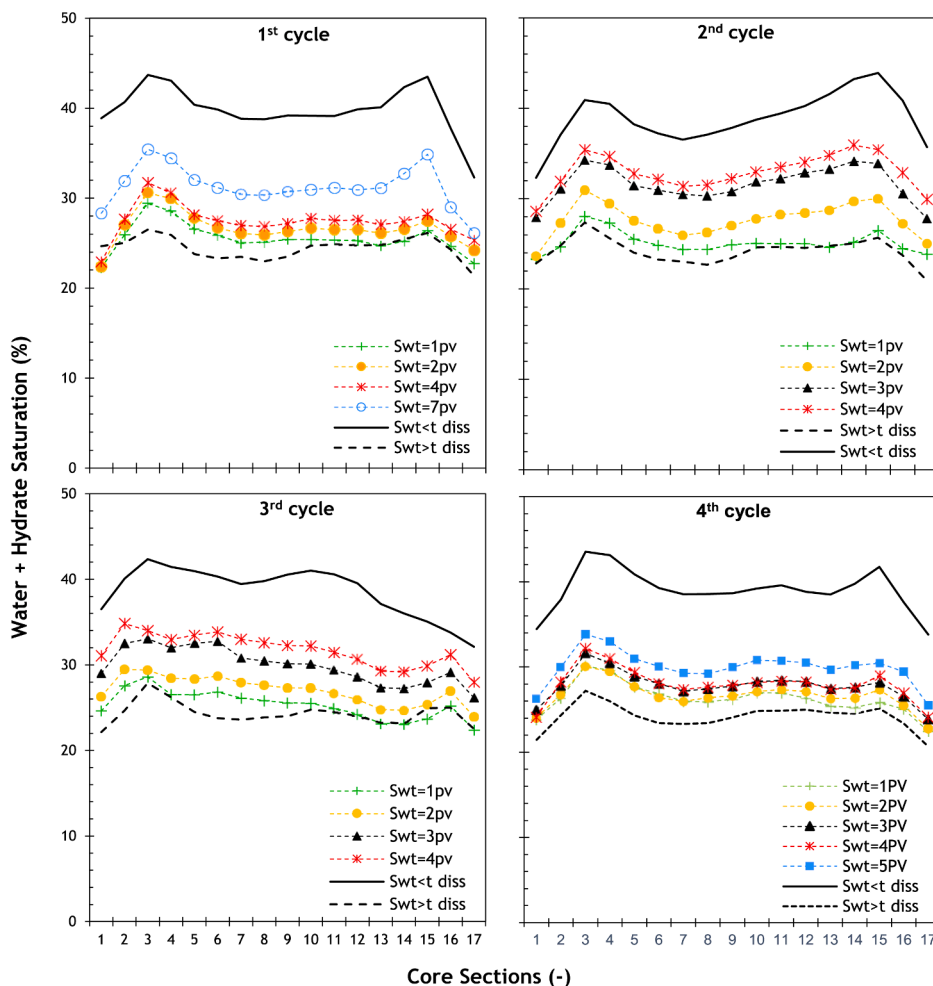


Fig. 8. Slice average saturations of water/hydrate along the length of the core during CO₂ injection and hydrate formation/dissociation across multiple cycles in E6. The time scale PV is equivalent to 44 min, based on the core pore volume and a CO₂ injection rate of 1 ml/min.

medical CT scan. Images were taken throughout the stages of hydrate formation, during stable hydrate conditions lasting up to one day, and following the decomposition step. Fig. 8 shows the slice-average saturation of water/hydrate along the 17 cm core during the four cycles of E6.

The data extracted from the CT scans of three selected water saturations are summarized in Table 2 and illustrated in Fig. 10. The results indicate an increase of approximately 10 %~15 % in final saturation of water + hydrate compared to the initial water saturation according to the flowchart represent in Fig. 9. This observation aligns well with the simulation results presented in Fig. 3.

Furthermore, considering the HydraFLASH conversion results and that the final stage reached a steady state without any further volume increase, it has been determined that the maximum water-to-hydrate conversion exceeded 98 %. Therefore, based on these findings, the density of hydrate emerged as a key factor. Under the specified experimental conditions, considering temperature, pressure, and excess CO₂ (due to the continuous CO₂ injection), HydraFLASH indicated a 21 % water-to-hydrate conversion and a hydrate density of 0.803 g/ml with a hydration number ranging from ~ 5.9 to 6.1 for structure sI. However, the CT experimental results suggest that to achieve this specific density (0.803 g/ml), a higher hydration number (>6.7) is required. Consequently, the CT results imply that the hydrate cavities are semi-filled with CO₂, which provides valuable insights into the hydrate composition under the dynamic CO₂ injection.

In Table 2, besides confirming the random process of hydrate nucleation, the observed variations in induction times between cycles attributed to the changing water history during dissociation [44,45]. For instance, in E7, hydrate was dissociated by thermal stimulation, and the core was kept at 293 K for a minimum of 40 h before fourth cycle of hydrate formation. These variations in thermal history are likely accountable for the discrepancies in induction time observed across the cycles. The results obtained indicate that induction times for CO₂ hydrate formation tend to increase with higher temperatures and longer dissociation durations.

The CO₂ injectivity index (J), calculated using Equation (8), which represents the ratio of the CO₂ injection rate (q_{CO_2}) to the differential pressure (dp), is depicted in Fig. 11 for different experiments (E1 to E8).

$$J = \frac{q_{CO_2}}{dp} \quad (8)$$

This data compares the impact of water saturation on the CO₂ injectivity index at the beginning of the growth phase, where a substantial amount of CO₂ is consumed during CO₂ dissolution and hydrate generation [46].

Table 2

Water saturation and CO₂ hydrate formation data with 1 ml/min CO₂ injection at 273.65 K and initial pressure of 3 MPa through the CT-scan.

water saturation (%)	Induction Time (hr)	Temp change with hydrate formation	Pressure drop by hydrate formation	CO ₂ hydrate saturation ^a (%)	CO ₂ hydrate volume (ml)
E6,1 (24.3)	3.9	1.42	0.85	38.7	12.88
E6,2 (24.4)	0.8	1.49	3.58	37.7	12.92
E6,3 (24.2)	0.3	1.54	3.66	37.4	12.83
E6,4 (24.3)	3.6	1.39	3.78	37.9	12.88
E7,1 (35.7)	0.7	1.85	0.16	48.5	18.80
E7,2 (31.4)	1.8	2.34	3.34	45.0	16.62
E7,3 (31.5)	2.3	2.90	4.47	46.8	16.73
E7,4 (31.4)	4.8	3.11	7.15	46.4	16.67
E8,1 (41.2)	5.0	1.48	56.4	54.7	21.89
E8,2 (39.6)	5.9	2.95	49.2	47.7	21.04
E8,3 (39.4)	2.1	2.99	49.9	48.4	20.93
E8,4 (39.5)	3.1	3.05	50.7	49.2	20.98

^a based on HydraFLASH prediction > 97 % water-to-hydrate conversion was assumed.

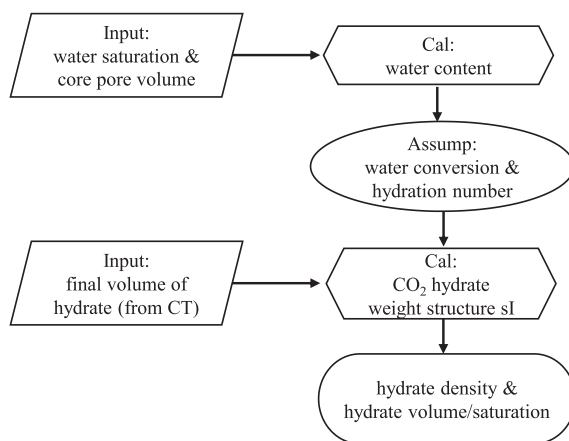


Fig. 9. Procedure of the estimation and calculation method for hydrate density and hydrate volume/saturation calculation based on the CT scan results.

Additionally, this figure highlights the effect of water hydrate memory on the injectivity of CO₂. The injectivity index in the first cycle of all experiments was higher than in the subsequent cycles due to the presence of water hydrate history in the secondary cycles. However, the experiment with an initial water saturation of 24.3 % (E6) was an exception, attributed to higher hydrate saturation compared to the other cycles, especially the third cycle. This finding indicates that hydrate saturation significantly impacts the injectivity index. According to the data reported in Table 2, in test E6, the hydrate saturation in the first cycle was substantially higher than in the subsequent cycles with the same water saturation level. Consequently, it was anticipated that the injectivity of the first cycle would be lower or comparable to that of the secondary cycles, even without considering water-memory effect [25]. Although the higher hydrate saturation in the first cycle of E7 and E8 compared to the secondary cycles was due to the higher initial water saturation of this cycle. Furthermore, in cycle 3 of experiment E6, the higher injectivity can be explained by the extended heating period for hydrate dissociation, which exceeded more than a day. This prolonged heating ensured the complete elimination of the hydrate history from the aqueous phase, thereby enhancing injectivity in the following cycles [47,48].

3.3. 3. Permeability change caused by hydrate formation

Two well-known Pang-Sharma [49] and Chen [50] models were used to predict the permeability reduction as a function of hydrate saturation. The purpose of selecting these two models was their inclusion of an adjustable parameter, which could be fine-tuned using the experimental data from this study to improve the accuracy of their predictions. The Pang-Sharma model includes a constant (β) that accounts for trapped particles deposit in the pores presented in equation (9):

$$\frac{k}{k_0} = \frac{1}{1 + \beta s_H} \quad (9)$$

The Chen model proposes a modified Corey model which includes a fitting parameter (c) that is depicted in equation (10):

$$\frac{k}{k_0} = (1 - s_H)e^{-cs_H} \quad (10)$$

In the above two equations, the brine permeability (k) values at each hydrate saturation were normalized by the initial permeability (k_0), the permeability before hydrate formation [51]. The obtained results indicated a decrease in normalized permeability with an increase in water or hydrate saturation, as shown in Fig. 12. The normalized permeability of the first cycle was compared with experimental data reported in the

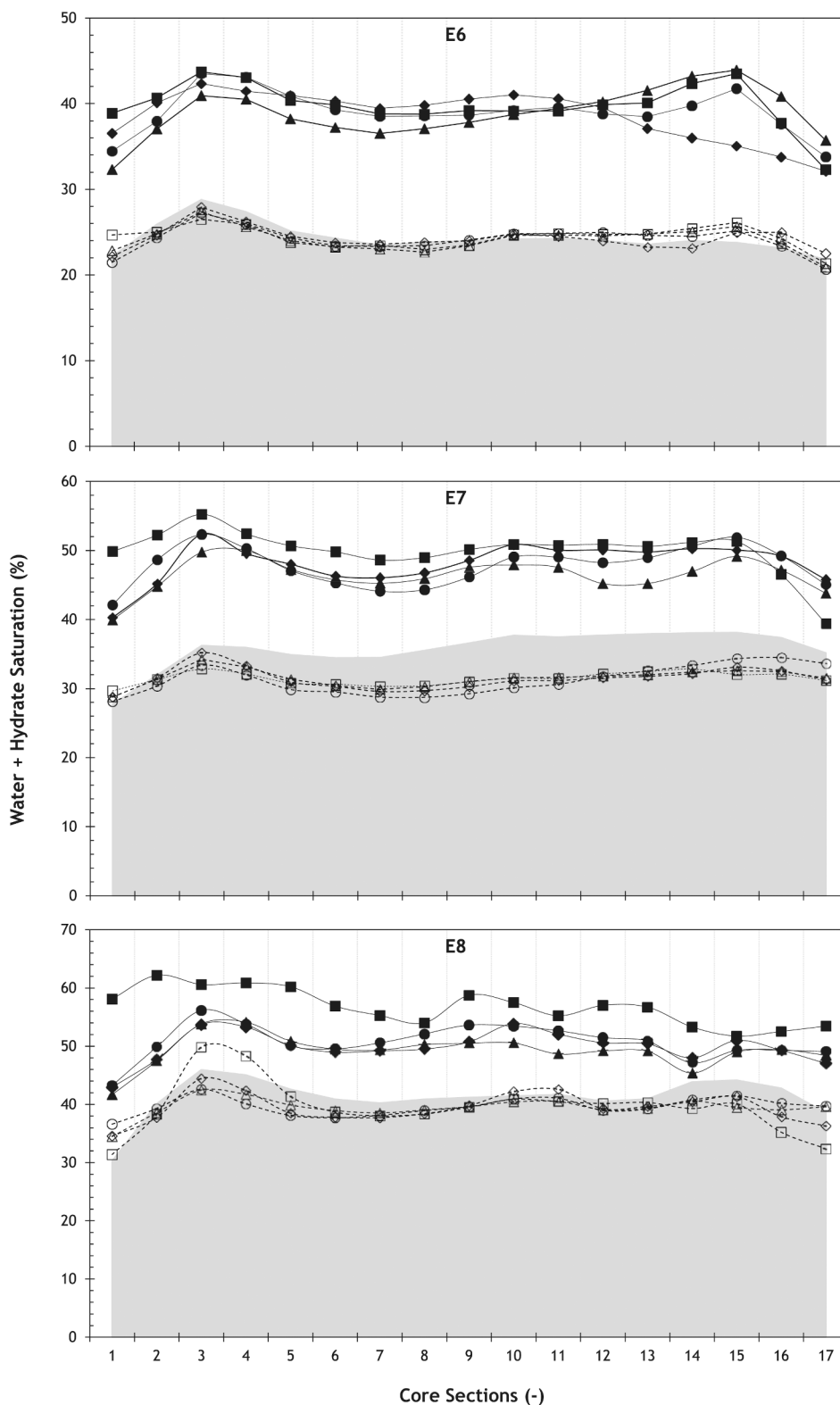


Fig. 10. Steady state water + hydrate saturation profiles along the length of the Bernheimer Sandrock core during four cycles of CO₂ hydrate formation/decomposition in E6, 7, and 8. The solid area shows the initial level of water saturation. ■: hydrate saturation of first cycle; ▲: hydrate saturation of second cycle; ◆: hydrate saturation of third cycle; ●: hydrate saturation of fourth cycle; □: water saturation after CO₂ hydrate dissociation of first cycle; △: water saturation after CO₂ hydrate dissociation of second cycle ◇: water saturation after CO₂ hydrate dissociation of third cycle ○: water saturation after CO₂ hydrate dissociation of fourth cycle. (The solid line represents the CO₂ hydrate formation; The dashed line represents the CO₂ hydrate dissociation).

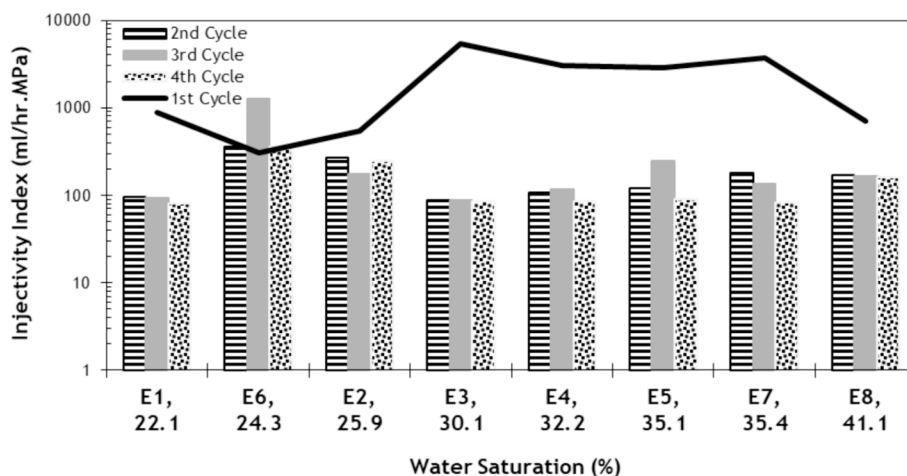


Fig. 11. Injectivity index at initial phase of rapid CO₂ consumption for different experiments.

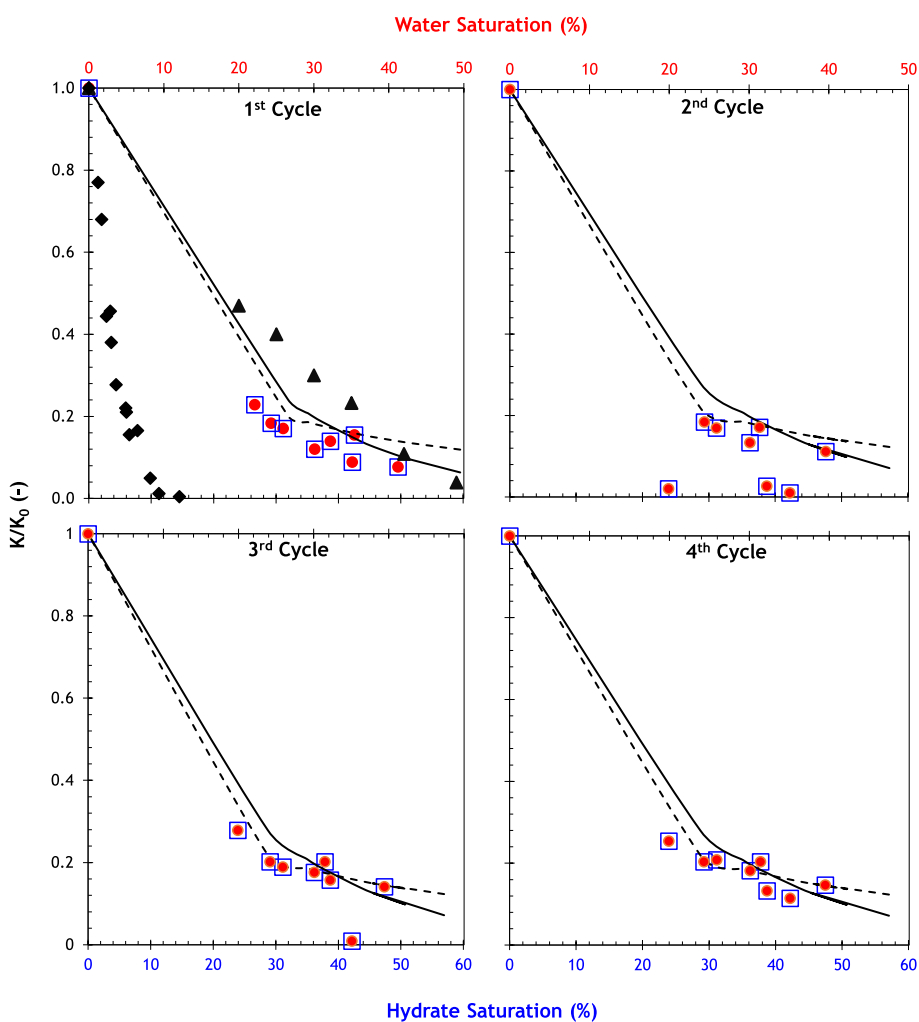


Fig. 12. Normalized permeability as a function of water/hydrate saturation – a compilation of experimental data compared to Pang Sharma and Chen models. (The blue hollow squares and red solid circles represent the normalized permeability as a function of hydrate saturation and water saturation, respectively (this study); solid triangles [52] and solid rhombus [53] depict experimental data; The dashed and solid lines correspond to the Pang-Sharma and Chen models respectively, adjusted using experimental data from this study).

literature and this trend showed good agreement with the literature [52,53]. Moreover, the experimental results for the studied range of water saturations demonstrate a close alignment with the predicted

values by the Pang-Sharma model, include a tuning parameter ($\beta = 0.15$) with a < 0.03 mean deviation from the experimental data.

As illustrated in Fig. 12, the experimental results indicate a notable

reduction in normalized permeability, approximately 80 %, after hydrate formation across all water saturation levels. This permeability reduction was more pronounced at higher water saturation (up to 90 %). However, the normalized permeability reduction resulting from CO₂ hydrate formation in porosity, driven by the memory effect, did not exhibit a significant change compared to the primary hydrate formation (first cycle without the memory effect). Furthermore, at some specific water saturations, e.g. 35 % (second and third cycle) and 22.1 % (second cycle), the primary flow channels were completely obstructed during some cycles. This blockage is attributed to alterations in water/hydrate distribution following previous hydrate dissociation. The observed significant decline in permeability highlights the profound impact of CO₂ hydrate formation on flow characteristics within porous media. This underscores the potential challenges and considerations inherent in CO₂ injection processes, especially when confronting the occurrence of complete blockage in flow channels during CO₂ injection. After conducting permeability tests with brine (1 wt% NaCl) following CO₂ hydrate dissociation, a slight reduction in permeability was observed compared to the initial permeability (around ~ 2.5 D). This reduction was attributed to salt dropout in some experiments, highlighting the influence of water memory on the salinity of brine during each hydrate formation/dissociation cycle. The observation arises from the fact that only water molecules enter the hydrate structure during formation, causing an increase in the salinity of the remaining brine. During hydrate dissociation, water molecules exit the lattice. However, due to limited mixing and a relatively slow rate of salt re-dissolution, the salinity of brine is effectively reduced during the following hydrate formation cycle. This reduction eventually leads to salt dropout or precipitation in the pores, impacting the pore permeability of sandstone [54]. Moreover, the decrease in salinity enhances CO₂ solubility in brine, promoting hydrate formation in subsequent cycles.

4. Conclusions

This research focuses on investigating the impact of water saturation and water memory on saturation and kinetics of CO₂ hydrate in porous media under dynamic CO₂ injection conditions. The study employs five distinct water saturations ranging from 20 % to 40 % each of which contains four cycles of hydrate formation/dissociation. The core flood experiments are conducted at 273.65 K and an initial pressure of 3 MPa, under a medical CT scan to monitor the onset of hydrate formation and dynamics of hydrate growth inside the core, allowing for the calculation of hydrate saturation profiles. The key findings include:

- The water-to-hydrate conversion ratio is unaffected by the level of water saturation within the examined range. This is due to continuous CO₂ injection, which maximizes the saturation of water with CO₂.
- There is a direct correlation between CO₂ hydrate saturation and water saturation levels, with a ratio of 1.21.
- The rate and total amount of water-to-hydrate conversion increases in the presence of water memory, confirming the existence of the water memory effect in porous media.
- Permeability is substantially reduced (approximately 80 %), as a result of hydrate formation at each water saturation. This reduction depends on the initial water saturation. However, the generated hydrate is insufficient to completely block the CO₂ flow path.
- The volume of water + hydrate phases increases during hydrate formation by 10–15 %, indicating a lower density for CO₂ hydrate (~ 0.9–0.8 g/ml) as compared to water. The estimated CO₂ hydrate density is reasonably consistent with data obtained from the HydraFLASH software.

CRedit authorship contribution statement

Mahnaz Aghajanloo: Writing – original draft, Software,

Methodology, Investigation. **Sadegh M. Taghinejad:** . **Denis Voskov:** Writing – review & editing, Supervision, Project administration, Conceptualization. **Rouhi Farajzadeh:** Writing – review & editing, Supervision, Project administration, Methodology, Investigation, Funding acquisition, Conceptualization.

Declaration of competing interest

The authors declare that they have no known competing financial interests or personal relationships that could have appeared to influence the work reported in this paper.

Data availability

Data will be made available on request.

Acknowledgement

Authors thank Shell Global Solutions International for granting permission to publish this work.

References

- [1] S.M. Benson, D.R. Cole, CO₂ Sequestration in Deep Sedimentary Formations, *Elements* 4 (5) (2008) 325–331, <https://doi.org/10.2113/gselements.4.5.325>.
- [2] K.Z. House, D.P. Schrag, C.F. Harvey, K.S. Lackner, Permanent carbon dioxide storage in deep-sea sediments, *Proc. Natl. Acad. Sci.* 103 (33) (2006) 12291–12295, <https://doi.org/10.1073/pnas.0605318103>.
- [3] L.J.R. Nunes, The Rising Threat of Atmospheric CO₂: A Review on the Causes, Impacts, and Mitigation Strategies, *Environments* 10 (4) (2023) 66. <https://www.mdpi.com/2076-3298/10/4/66>.
- [4] J.M. Ketzer, R.S. Iglesias, S. Einloft, Reducing Greenhouse Gas Emissions with CO₂ Capture and Geological Storage, in: W.-Y. Chen, J. Seiner, T. Suzuki, M. Lackner (Eds.), *Handbook of Climate Change Mitigation*, Springer, US, 2012, pp. 1405–1440, https://doi.org/10.1007/978-1-4419-7991-9_37.
- [5] P. Roy, A. Mohanty, M. Misra, Prospects of carbon capture, utilization and storage for mitigating climate change, *Environmental Science: Advances* 2 (2023), <https://doi.org/10.1039/D2VA00236A>.
- [6] S. Bachu, Sequestration of CO₂ in geological media: criteria and approach for site selection in response to climate change, *Energy Convers. Manage.* 41 (9) (2000) 953–970, [https://doi.org/10.1016/S0196-8904\(99\)00149-1](https://doi.org/10.1016/S0196-8904(99)00149-1).
- [7] T. Dance, Assessment and geological characterisation of the CO₂CRC Otway Project CO₂ storage demonstration site: From prefeasibility to injection, *Mar. Pet. Geol.* 46 (2013) 251–269, <https://doi.org/10.1016/j.marpetgeo.2013.06.008>.
- [8] C.M. Oldenburg, S.M. Benson, CO₂ Injection for Enhanced Gas Production and Carbon Sequestration. SPE International Petroleum Conference and Exhibition in Mexico, 2002.
- [9] Y. Song, S. Jun, Y. Na, K. Kim, Y. Jang, J. Wang, Geomechanical challenges during geological CO₂ storage: A review, *Chem. Eng. J.* 456 (2023) 140968, <https://doi.org/10.1016/j.cej.2022.140968>.
- [10] J. Underschultz, C. Boreham, T. Dance, L. Stalker, B. Freifeld, D. Kirste, J. Ennis-King, CO₂ storage in a depleted gas field: An overview of the CO₂CRC Otway Project and initial results, *International Journal of Greenhouse Gas Control - INT J GREENH GAS CONTROL* 5 (2011) 922–932, <https://doi.org/10.1016/j.ijggc.2011.02.009>.
- [11] C. Oldenburg, Joule-Thomson cooling due to CO₂ injection into natural gas reservoirs, *Lawrence Berkeley National Laboratory* 48 (2006), <https://doi.org/10.1016/j.enconman.2007.01.010>.
- [12] H. Hoteit, M. Fahs, M.R. Soltanian, Assessment of CO₂ Injectivity During Sequestration in Depleted Gas Reservoirs, *Geosciences* 9 (5) (2019) 199. <https://www.mdpi.com/2076-3263/9/5/199>.
- [13] M. Wapperom, X. Lyu, D. Voskov, Accurate Modeling of near-Wellbore Effects Induced by Supercritical CO₂ Injection. 2022 (1) (2022) 1–13, <https://doi.org/10.3997/2214-4609.202244092>.
- [14] M. Aghajanloo, L. Yan, S. Berg, D. Voskov, R. Farajzadeh, Impact of CO₂ Hydrates on Injectivity During CO₂ Storage in Depleted Gas Fields: A Literature Review, *Gas Science and Engineering Journal* (2023), <https://doi.org/10.2139/ssrn.4674558>.
- [15] C. Chesnokov, a. F., Rouhi and Kahrobaei, Siavash and Snippe, Jeroen and Bedrikovetski, Pavel., Analytical Model for Joule-Thomson Cooling Under Heat Exchange During CO₂ Storage in Geological Formations, *SSRN* (2023), <https://doi.org/10.2139/ssrn.4441293>.
- [16] T.H. Le Goff, F. Lagarde, S. Thibeau, A. Brisset, CO₂ Injection in Depleted Reservoirs: Analysis, *Modelling 15th Greenhouse Gas Control Technologies Conference*. (2021).
- [17] H. Pahlavanzadeh, S. Nouri, M. Aghajanloo, A.H. Mohammadi, S. Mohammadi, Experimental measurements and thermodynamic modeling of hydrate dissociation conditions for CO₂ + THF + MgCl₂ + water systems, *Fluid Phase Equilib.* 564 (2023) 113626, <https://doi.org/10.1016/j.fluid.2022.113626>.

- [18] D. Sun, P. Englezos, CO₂ storage capacity in laboratory simulated depleted hydrocarbon reservoirs – Impact of salinity and additives, *J. Nat. Gas Sci. Eng.* 35 (2016) 1416–1425, <https://doi.org/10.1016/j.jngse.2016.03.043>.
- [19] D. Akindipe, S. Saraji, M. Piri, Salt precipitation in carbonates during supercritical CO₂ injection: A pore-scale experimental investigation of the effects of wettability and heterogeneity, *Int. J. Greenhouse Gas Control* 121 (2022) 103790, <https://doi.org/10.1016/j.jggc.2022.103790>.
- [20] O. Hansen, D. Gilding, B. Nazarian, B. Osdal, P. Ringrose, J.-B. Kristoffersen, O. Eiken, H. Hansen, Snøhvit: The History of Injecting and Storing 1 Mt CO₂ in the Fluvial Tubåen Fm, *Energy Procedia* 37 (2013) 3565–3573, <https://doi.org/10.1016/j.egypro.2013.06.249>.
- [21] J. Gauteplass, S. Almennigen, T. Barth, G. Erslund, Hydrate Plugging and Flow Remediation during CO₂ Injection in Sediments, *Energies* 13 (17) (2020) 4511. <https://www.mdpi.com/1996-1073/13/17/4511>.
- [22] R.P. Singh, K.S. Shekhawat, M.K. Das, K. Muralidhar, Geological sequestration of CO₂ in a water-bearing reservoir in hydrate-forming conditions, *Oil Gas Sci. Technol. – Rev. IFP Energies Nouvelles* 75 (2020) 51, <https://doi.org/10.2516/ogst/2020038>.
- [23] L. Wang, M. Dou, Y. Wang, Y. Xu, Y. Li, Y. Chen, L. Li, A Review of the Effect of Porous Media on Gas Hydrate Formation, *ACS Omega* 7 (38) (2022) 33666–33679, <https://doi.org/10.1021/acsomega.2c03048>.
- [24] B.-B. Ge, D.-L. Zhong, Y.-Y. Lu, Influence of water saturation and particle size on methane hydrate formation and dissociation in a fixed bed of silica sand, *Energy Procedia* 158 (2019) 5402–5407, <https://doi.org/10.1016/j.egypro.2019.01.623>.
- [25] Y. Wei, N. Maeda, Mechanisms of the memory effect of clathrate hydrates, *Chem. Eng. Sci.* 270 (2023) 118538, <https://doi.org/10.1016/j.ces.2023.118538>.
- [26] W. Lenstra, J. Van Doorn, B. Verheggen, E. Sahan, A. Boersma, *State of the art of mitigation & relation mitigation/adaptation*, Knowledge for Climate Programme Office, 2009.
- [27] A.A. Eftekhari, R. Farajzadeh, Effect of Foam on Liquid Phase Mobility in Porous Media, *Sci. Rep.* 7 (1) (2017) 43870, <https://doi.org/10.1038/srep43870>.
- [28] L. Shi, J. Li, Y. He, J. Lu, Z. Long, D. Liang, Memory effect test and analysis in methane hydrates reformation process, *Energy* 272 (2023) 127153, <https://doi.org/10.1016/j.energy.2023.127153>.
- [29] V. Dhamu, M.F. Qureshi, S. Abubakar, A. Usadi, T.A. Barckholtz, A.B. Mhadeshwar, P. Linga, Investigating High-Pressure Liquid CO₂ Hydrate Formation, Dissociation Kinetics, and Morphology in Brine and Freshwater Static Systems, *Energy Fuel* 37 (12) (2023) 8406–8420, <https://doi.org/10.1021/acs.energyfuels.3c01089>.
- [30] M. Boon, H. Hajibeygi, Experimental characterization of H₂/water multiphase flow in heterogeneous sandstone rock at the core scale relevant for underground hydrogen storage (UHS), *Sci. Rep.* 12 (1) (2022) 14604, <https://doi.org/10.1038/s41598-022-18759-8>.
- [31] L. Lei, Y. Seol, High-Saturation Gas Hydrate Reservoirs—A Pore Scale Investigation of Their Formation From Free Gas and Dissociation in Sediments, *J. Geophys. Res. Solid Earth* 124 (2019), <https://doi.org/10.1029/2019JB018243>.
- [32] J. Wang, Y. Tie, Z. Liu, L. Zhang, H. Jiang, P. Guo, Effects of Different Factors on Methane Hydrate Formation Using a Visual Wellbore Simulator, *ACS Omega* 7 (27) (2022) 23147–23155, <https://doi.org/10.1021/acsomega.2c00903>.
- [33] E.D. Sloan, *Clathrate Hydrates of Natural Gases*, Second Edition, Taylor & Francis, Revised and Expanded, 1998 <https://books.google.nl/books?id=jBaLcv6qKnsC>.
- [34] P.M. Rodger, Methane hydrate: melting and memory, *Ann. N. Y. Acad. Sci.* 912 (1) (2000) 474–482.
- [35] Z. Wen, Y. Yao, W. Luo, X. Lei, Memory effect of CO₂-hydrate formation in porous media, *Fuel* 299 (2021) 120922, <https://doi.org/10.1016/j.fuel.2021.120922>.
- [36] E.D. Sloan, S. Subramanian, P. Matthews, J. Lederhos, A. Khokhar, Quantifying hydrate formation and kinetic inhibition, *Ind. Eng. Chem. Res.* 37 (8) (1998) 3124–3132.
- [37] H. Thompson, A.K. Soper, P. Buchanan, N. Aldiwan, J.L. Creek, C.A. Koh, Methane hydrate formation and decomposition: Structural studies via neutron diffraction and empirical potential structure refinement, *J. Chem. Phys.* 124 (16) (2006).
- [38] Y. Seol, T. Kneafsey, *Fluid Flow Through Heterogeneous Methane Hydrate Bearing, Observations Using X-ray CT Scanning, Sand*, 2008.
- [39] M. Vasheghani Farahani, X. Guo, L. Zhang, M. Yang, A. Hassanpouryouzband, J. Zhao, J. Yang, Y. Song, B. Tohidi, Effect of thermal formation/dissociation cycles on the kinetics of formation and pore-scale distribution of methane hydrates in porous media: a magnetic resonance imaging study [10.1039/D0SE01705A], *Sustainable Energy Fuels* 5 (5) (2021) 1567–1583, <https://doi.org/10.1039/D0SE01705A>.
- [40] E.V.L. Rees, T.J. Kneafsey, Y. Seol, Methane Hydrate Distribution from Prolonged and Repeated Formation in Natural and Compacted Sand Samples: X-Ray CT Observations, *Journal of Geological Research* 2011 (2011) 791815, <https://doi.org/10.1155/2011/791815>.
- [41] Y. Lu, H. Wang, Q. Li, X. Lv, Y. Ge, L. Zhang, J. Zhao, L. Yang, Y. Song, CO₂ storage behavior via forming hydrate from N₂/CO₂ gas mixtures in the presence of initial SI CO₂ hydrate seeds, *Chem. Eng. J.* 450 (2022) 138001, <https://doi.org/10.1016/j.ces.2022.138001>.
- [42] J. Parent, P. Bishnoi, Investigations into the nucleation behaviour of methane gas hydrates, *Chem. Eng. Commun.* 144 (1) (1996) 51–64.
- [43] P. Servio, P. Englezos, Morphology of methane and carbon dioxide hydrates formed from water droplets, *AIChE J.* 49 (1) (2003) 269–276.
- [44] M.L. Martinez de Baños, O. Carrier, P. Bouriat, D. Broseta, Droplet-based millifluidics as a new tool to investigate hydrate crystallization: Insights into the memory effect, *Chem. Eng. Sci.* 123 (2015) 564–572, <https://doi.org/10.1016/j.ces.2014.11.018>.
- [45] H. Sefidroodi, E. Abrahamsen, M.A. Kelland, Investigation into the strength and source of the memory effect for cyclopentane hydrate, *Chem. Eng. Sci.* 87 (2013) 133–140, <https://doi.org/10.1016/j.ces.2012.10.018>.
- [46] D. Gootam, N. Gaikwad, R. Kumar, N. Kaisare, Modeling Growth Kinetics of Methane Hydrate in Stirred Tank Batch Reactors, *ACS Engineering Au* 1 (2) (2021) 148–159, <https://doi.org/10.1021/acseengineeringau.1c00012>.
- [47] X. Kou, J.-C. Feng, X.-S. Li, Y. Wang, Z.-Y. Chen, Memory effect of gas hydrate: Influencing factors of hydrate reformation and dissociation behaviors*, *Appl. Energy* 306 (2022) 118015 <https://doi.org/10.1016/j.apenergy.2021.118015>.
- [48] Y. Li, N. Wu, C. He, Z. Sun, Z. Zhang, X. Hao, Q. Chen, Q. Bu, C. Liu, J. Sun, Nucleation probability and memory effect of methane-propane mixed gas hydrate, *Fuel* 291 (2021) 120103, <https://doi.org/10.1016/j.fuel.2020.120103>.
- [49] S. Pang, M.M. Sharma, A Model for Predicting Injectivity Decline in Water- Injection Wells, *SPE Form. Eval.* 12 (03) (1997) 194–201, <https://doi.org/10.2118/28489-pa>.
- [50] X. Chen, R. Verma, D.N. Espinoza, M. Prodanović, Pore-scale determination of gas relative permeability in hydrate-bearing sediments using X-ray computed microtomography and lattice Boltzmann method, *Water Resour. Res.* 54 (1) (2018) 600–608.
- [51] N. Mahabadi, S. Dai, Y. Seol, J. Jang, Impact of hydrate saturation on water permeability in hydrate-bearing sediments, *J. Pet. Sci. Eng.* 174 (2019) 696–703, <https://doi.org/10.1016/j.petrol.2018.11.084>.
- [52] A. Kumar, B. Maini, P.R. Bishnoi, M. Clarke, O. Zatschina, S. Srinivasan, Experimental determination of permeability in the presence of hydrates and its effect on the dissociation characteristics of gas hydrates in porous media, *J. Pet. Sci. Eng.* 70 (1) (2010) 114–122, <https://doi.org/10.1016/j.petrol.2009.10.005>.
- [53] P. Shen, G. Li, B. Li, X. Li, Y. Liang, Q. Lv, Permeability measurement and discovery of dissociation process of hydrate sediments, *J. Nat. Gas Sci. Eng.* 75 (2020) 103155, <https://doi.org/10.1016/j.jngse.2020.103155>.
- [54] S.M. Roels, N. El Chatib, C. Nicolaidis, P.L.J. Zitha, Capillary-Driven Transport of Dissolved Salt to the Drying Zone During CO₂ Injection in Homogeneous and Layered Porous Media, *Transp. Porous Media* 111 (2) (2016) 411–424, <https://doi.org/10.1007/s11242-015-0601-y>.